Single-energy partial wave analysis for π^0 photoproduction on the proton with fixed-t analyticity imposed

H. Osmanović,[1,*] M. Hadžimehmedović,[1] R. Omerović,[1] J. Stahov,[1] M. Gorchtein,[2] V. Kashevarov,[2] K. Nikonov,[2,†] M. Ostrick,[2] L. Tiator,[2] and A. Švarc[3,4]

[1]*University of Tuzla, Faculty of Natural Sciences and Mathematics, Univerzitetska 4, 75000 Tuzla, Bosnia and Herzegovina*
[2]*Institut für Kernphysik, Johannes Gutenberg-Universität Mainz, D-55099 Mainz, Germany*
[3]*Rudjer Bošković Institute, Bijenička cesta 54, P.O. Box 180, 10002 Zagreb, Croatia*
[4]*Tesla Biotech, Mandlova 7, 10002 Zagreb, Croatia*

(Received 16 August 2019; published 21 November 2019)

High-precision data of the $\gamma p \to \pi^0 p$ reaction from its threshold up to $W = 1.9$ GeV have been used in order to perform a single-energy partial-wave analysis with minimal model dependence. Continuity in energy was achieved by imposing constraints from fixed-t analyticity in an iterative procedure. Reaction models were only used as starting point in the very first iteration. We demonstrate that, with this procedure, partial-wave amplitudes can be obtained which show only a minimal dependence on the initial model assumptions.

DOI: 10.1103/PhysRevC.100.055203

I. INTRODUCTION

The excitation spectra of nucleons have been studied since the 1950s and provided important pieces of information during the discovery of quarks and color charge. However, despite of this long history, the spectrum is still not fully established and much less understood. At high energies ($W > 2$ GeV), various quark models and lattice QCD predict an almost exponential increase in the density of states which could so far not be confirmed experimentally ("missing resonance problem"). In this paper, we discuss the lower-energy range $W < 2$ GeV where most analyses agree on the number of states, however, with sizable uncertainties in the decay properties and even in the excitation energies. Because of their extremely short lifetime, excited nucleons appear as resonance poles in complex partial-wave scattering amplitudes. The reliable and unambiguous determination of these amplitudes is a central task which requires both precision measurements of several spin-dependent observables and sophisticated analysis methods. Major progress was made in meson photo- and electroproductions due to the availability of high intensity polarized beams and polarized targets in combination with 4π-detector systems. In our analysis, we use both polarized and unpolarized data obtained at ELSA, GRAAL, JLab, and MAMI. Data with unprecedented quality and quantity are available, in particular, for photoproduction of pions.

Theoretical single or multichannel models were developed and used to determine the resonance parameters. These approaches are called energy-dependent (ED) analyses because the energy dependence of amplitudes is parametrized in terms of resonant and nonresonant contributions. The model parameters are estimated by fits to the data. Ideally, such models should respect fundamental constraints, such as analyticity, unitarity, and crossing symmetry. On the other hand, the computational effort should be sufficiently small to allow for detailed systematic studies during the complex fitting procedures. In practice, compromises are necessary, and, in genera,l the extracted multipole amplitudes and resonance parameters vary from model to model. A recent comparison of the prominent ED models (Bonn-Gatchina (BnGa) [1], Jülich-Bonn (JüBo) [2], George Washington University (SAID) [3], and Mainz (MAID) [4]) has been performed in Ref. [5]. There, for the case of the $\gamma p \to \pi^0 p$ reaction, it has been demonstrated that the model dependence can be reduced and that multipoles obtained in different analyses start to converge when all modern polarized and unpolarized data are taken into account.

In so-called energy-independent or single-energy (SE) approaches a truncated partial-wave expansion is fitted to the measured angular distributions independently at each individual energy bin without using a reaction model. At first sight, this method seems to provide a direct connection between experimental data and multipole amplitudes. However, it has been demonstrated that possible ambiguities can only partially be resolved by high-quality experimental data alone [6–8]. All observables remain unchanged if, at each energy and angular bin, the reaction amplitudes are multiplied by an overall phase $\phi(W, \theta)$. This continuum ambiguity prevents a unique projection to multipoles. In Ref. [9], this has been studied in detail, and it was shown that a single-energy partial-wave analysis is discontinuous in energy unless this phase is constrained by additional theoretical input.

In the simple case of pion production close to threshold and in the energy region of the $\Delta(1232)$ resonance where only a few partial waves contribute and unitarity provides

*hedim.osmanovic@untz.ba
†Present address: Helmholtz-Institut für Strahlen- und Kernphysik, University of Bonn, Bonn, Germany.

strong constraints in the form of Migdal-Watson's theorem [10,11], model-independent multipole analyses were possible [12–14]. However, in all analyses at higher energies, the fits were constrained to a parametrization of the amplitudes given by a preferred reaction model (e.g., Refs. [15–17]). These kinds of analyses are useful in order to study the consistency of the energy-dependent parametrization of a model, however, they do not provide independent multipole amplitudes.

In Ref. [18], we have developed a method to impose analyticity of the reactions' amplitudes in the Mandelstam variable s at a fixed value of the variable t in an iterative procedure. A reaction model is only necessary as a starting point in the very first iteration. We have applied this method to the $\gamma p \to \eta p$ reaction and demonstrated that, indeed, single-energy solutions can be obtained which do not have discontinuities in their energy dependence. Remaining ambiguities were traced back to limitations in the database and different overall phases $\phi(W,\theta)$ of the initial reaction models. In this paper, we apply the method to the $\gamma p \to \pi^0 p$ reaction, and the extension to all charge channels with the aim to carry out the full isospin reconstruction is in progress. On the one side, pion production is more complicated than η production because both excitations with isospin $I = 1/2$ (N) and $I = 3/2$ (Δ), contribute in the same $\pi^0 p$ multipoles. On the other side, much more experimental data are available, and the phases in different models are stronger constrained than in η production.

The paper is organized as follows. In Sec. II, we briefly describe the formalism. In Sec. III, we comment on the experimental data that were used in our analysis and present the single-energy multipoles for different starting solutions. In Sec. IV, we compare our results with experimental data and give suggestions for further measurements in order to obtain a unique partial-wave amplitude (PWA). Finally, in the appendices, we give basic formulas for kinematics and polarization observables in different representations.

II. FORMALISM

In this paper, we apply the fixed-t analyticity constraining method for single-energy partial-wave analysis in $p(\gamma,\pi^0)p$ that we developed previously and applied to η photoproduction on the proton [18]. All details are described in our previous paper, and only some important issues as the iterated fitting procedure are repeated here. The kinematics for pion photoproduction is presented in Appendix A, cross sections and polarization observables used in our analysis are defined in Appendix B, and expressions in terms of Chew-Goldberger-Low-Nambu (CGLN) amplitudes and helicity amplitudes are listed in Appendix C.

Pseudoscalar meson photoproduction on the nucleon as $p(\gamma,\eta)p$ and $p(\gamma,\pi^0)p$ are fully described with four invariant amplitudes, e.g., $A_i(\nu,t)$, $i = 1,\ldots,4$, where $\nu = \frac{s-u}{4m_N}$ and t are Mandelstam variables, see Appendix A. For a close connection among amplitudes and observables, spin (CGLN) amplitudes $F_i(W,\theta)$, $i = 1,\ldots,4$ and helicity amplitudes $H_i(W,\theta)$, $i = 1,\ldots,4$ are defined in the meson-nucleon c.m. frame, where W is the total c.m. energy and θ is the c.m. angle of the outgoing meson. Although, for $N(\gamma,\eta)N$, the isospin in the final ηN system is $\frac{1}{2}$, and only two channels, proton and neutron, exist, in pion photoproduction, the total isospin is either $\frac{1}{2}$ or $\frac{3}{2}$, and four channels $p(\gamma,\pi^0)p$, $n(\gamma,\pi^0)n$, $p(\gamma,\pi^+)n$, and $n(\gamma,\pi^-)p$ are possible. In a future (ongoing) work, a full isospin analysis will be performed using our fixed-t method. Here, we concentrate only on $p(\gamma,\pi^0)p$ and, therefore, we can ignore the isospin aspect here, and treat everything just like η photoproduction with π^0 as a "light η meson."

In this paper, we introduce fixed-t analyticity in the SE PWA to ensure the continuity of PWA solutions following the method developed for η photoproduction in Ref. [18]. Namely, if one performs a SE PWA freely, one actually uses all available data on observables $O(W_{\text{fixed}},\theta)$ at one isolated energy at different angles without paying any attention to what is happening at neighboring energies. However, as has been shown in Ref. [9], continuum ambiguity (invariance of reaction amplitudes to the rotation with arbitrary real energy and an angle-dependent phase) enables multiplicity of equivalent but different PWA solutions at one energy with a different reaction amplitude phase, so if no continuity of the phase is imposed when we move from one energy to another one, the solution is automatically discontinuous as each different phase gives different sets of partial waves. One elegant solution to this problem is imposing the analyticity at fixed t and that automatically means continuity in energy as well. To do so, first we have to obtain reaction amplitudes in the t variable which describe the used database but which are at the same time continuous at fixed t. To achieve that, we have to perform an amplitude reconstruction of observables not in the $O(W_{\text{fixed}},\theta)$ form but in the $O(t_{\text{fixed}},W)$ form. The first step is to interpolate the existing data to predetermined fixed-t values. This procedure, called a fixed-t data binning, is, in detail, described in Ref. [18]. As a second step, we have to fit these data with a continuous function. As we demand a minimal model dependence, instead of using theoretical models, we use the Pietarinen expansion method first applied in the PWA of πN elastic-scattering data [19,20] to describe the reaction amplitudes in fixed t. We start with an arbitrary solution and find a fixed-t solution in such a way that our results do not deviate much from the starting solution using penalty function techniques. We then take the obtained continuous amplitudes as a constraint in the SE PWA again using penalty function techniques to impose continuity in energy. In this way, we obtain a SE solution, which at the same time, describes the measured data and is continuous. This solution is different from the starting solution. With the obtained results, we go back to the fixed-t amplitude analysis and use it as a constraint. We continue this iterative procedure as long as the result does not change much, and this typically happens after three to four iterations. The final result is continuous in energy. Details of the procedure are given in Refs. [18,19,21].

The method consists of two separate analyses, the fixed-t amplitude analysis (FT AA) and the single-energy partial-wave analysis (SE PWA). The two analyses are coupled in such a way that the results from FT AA are used as a constraint in the SE PWA and vice versa in an iterative procedure. It has not been proven, but it is extensively tested

in πN elastic fixed-t constrained SE PWA [19] and since then recommended for other processes.

Step 1. Constrained FT AA is performed by minimizing the form

$$X^2 = \chi^2_{\mathrm{FT\,data}} + \chi^2_{\mathrm{cons}} + \Phi_{\mathrm{conv}}, \tag{1}$$

where χ^2_{cons} is a constraining term given by

$$\chi^2_{\mathrm{cons}} = q_{\mathrm{cons}} \sum_{k=1}^{4} \sum_{i=1}^{N^E} \left(\frac{\mathrm{Re}\, H_k(E_i)^{\mathrm{fit}} - \mathrm{Re}\, H_k(E_i)^{\mathrm{cons}}}{\varepsilon^{\mathrm{Re}}_{k,i}} \right)^2 + q_{\mathrm{cons}} \sum_{k=1}^{4} \sum_{i=1}^{N^E} \left(\frac{\mathrm{Im}\, H_k(E_i)^{\mathrm{fit}} - \mathrm{Im}\, H_k(E_i)^{\mathrm{cons}}}{\varepsilon^{\mathrm{Im}}_{k,i}} \right)^2. \tag{2}$$

H_k^{cons}'s are helicity amplitudes from the SE PWA in the previous iteration. In a first iteration, H_k^{cons}'s are calculated from the initial PWA solution (MAID, SAID, BnGa, and JüBo). H_k^{fit}'s are values of helicity amplitudes H_k calculated from coefficients in Pietarinen's expansions, which are parameters of the fit. N^E is the number of energies for a given value of t, and q_{cons} is an adjustable weight factor. $\varepsilon^{\mathrm{Re}}_{k,i}$ and $\varepsilon^{\mathrm{Im}}_{k,i}$ are errors of real and imaginary parts of the corresponding helicity amplitudes. In our analysis, we take $\varepsilon^{\mathrm{Re}}_{k,i} = \varepsilon^{\mathrm{Im}}_{k,i} = 1$.

Step 2. The constrained SE PWA is performed by minimizing the form

$$X^2 = \chi^2_{\mathrm{SE\,data}} + \chi^2_{\mathrm{FT}} + \Phi_{\mathrm{trunc}}, \tag{3}$$

where the additional term χ^2_{FT} contains the helicity amplitudes from the FT AA in Step 1,

$$\chi^2_{\mathrm{FT}} = q_{\mathrm{cons}} \sum_{k=1}^{4} \sum_{i=1}^{N^C} \left(\frac{\mathrm{Re}\, H_k(\theta_i)^{\mathrm{fit}} - \mathrm{Re}\, H_k(\theta_i)^{\mathrm{FT}}}{\varepsilon^{\mathrm{Re}}_{k,i}} \right)^2 + q_{\mathrm{cons}} \sum_{k=1}^{4} \sum_{i=1}^{N^C} \left(\frac{\mathrm{Im}\, H_k(\theta_i)^{\mathrm{fit}} - \mathrm{Im}\, H_k(\theta_i)^{\mathrm{FT}}}{\varepsilon^{\mathrm{Im}}_{k,i}} \right)^2.$$

N^C is the number of angles for a given energy E and the values θ_i are obtained for a corresponding value of t using Eq. (A15).

Step 3. Use resulting multipoles obtained in Step 2, and calculate helicity amplitudes which serve as a constraint in Step 1.

$\chi^2_{\mathrm{FT\,data}}$ and $\chi^2_{\mathrm{SE\,data}}$ are standard χ^2 functions calculating the weighted deviations between theory and experiment, and Φ_{conv} and Φ_{trunc} are penalty functions that are described in Ref. [18]. In Step 1 for the FT AA, the energy-dependent helicity amplitudes $H_k(E_i)^{\mathrm{fit}}$ are parametrized with Pietarinen functions where the expansion coefficients are the fit parameters. In Step 2 for the SE PWA, the angle-dependent helicity amplitudes $H_k(\theta_i)^{\mathrm{fit}}$ are parametrized with Legendre functions and multipoles where the multipoles are the fit parameters. An iterative minimization scheme which accomplishes point-to-point continuity in energy is given in Fig. 1.

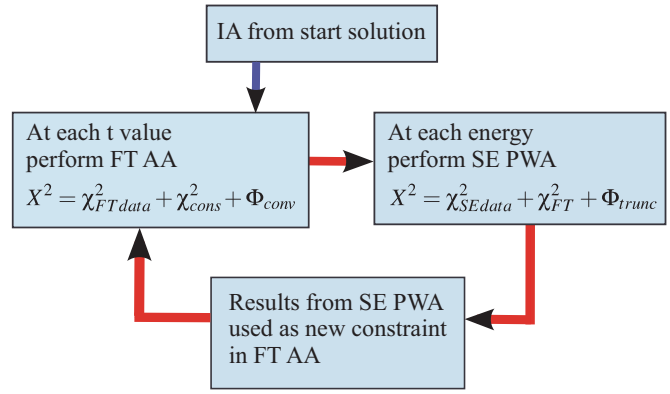

FIG. 1. Iterative minimization scheme which achieves point-to-point continuity in energy using fixed-t analyticity as a constraint.

III. RESULTS

A. π^0 photoproduction database

The majority of experimental data on the $\gamma p \to \pi^0 p$ reaction were obtained with energy-tagged photon beams and large solid angle electromagnetic calorimeters with a high efficiency for a detection of the two photons from the $\pi^0 \to \gamma\gamma$ decay. We used data from the A2 Collaboration at the Mainz Microtron MAMI [13,22–27], the CBELSA/TAPS Collaboration at ELectron Stretcher and Accelerator ELSA [28–30], and the GRAAL Detector at the European Synchrotron Radiation Facility [31].

We used, in the fit, the latest experimental data for eight observables from the SAID database [32] that have maximal angular covering and minimal energy binning at energy $W < 1.9$ GeV. The most accurate data in this energy region are available for differential cross sections (MAMI [13] and MAMI [22]): 20 or 30 bins covering the full angle range at

TABLE I. Experimental data from A2@MAMI, DAPHNE/MAMI, CBELSA/TAPS, and GRAAL Collaborations used in our SE PWA.

Observables	N	W (MeV)	N_E	Reference
σ_0	5240	1075–1541	262	A2@MAMI(2013) [13]
	3930	1132–1895	246	A2@MAMI(2015) [22]
Σ	528	1074–1215	54	A2@MAMI(2013) [13]
	357	1150–1310	21	A2@MAMI(2001) [23]
	471	1383–1922	31	GRAAL(2005) [31]
T	469	1295–1895	34	A2@MAMI(2016) [24]
	157	1462–1620	8	CBELSA/TAPS(2014) [28]
$T\sigma_0$	4500	1074–1291	250	A2@MAMI(2015) [25]
P	157	1462–1620	8	CBELSA/TAPS(2014) [28]
$E\sigma_0$	139	1201–1537	24	DAPHNE/MAMI(2001) [23]
E	88	1481–1951	5	CBELSA/TAPS(2014) [29]
	480	1129–1878	40	A2@MAMI(2015) [26]
F	469	1295–1895	34	A2@MAMI(2016) [24]
$F\sigma_0$	4500	1074–1291	250	A2@MAMI(2015) [25]
G	3	1232	1	DAPHNE/MAMI(2005) [27]
	318	1430–1727	19	CBELSA/TAPS(2012) [30]
H	157	1462–1620	8	CBELSA/TAPS(2014) [28]

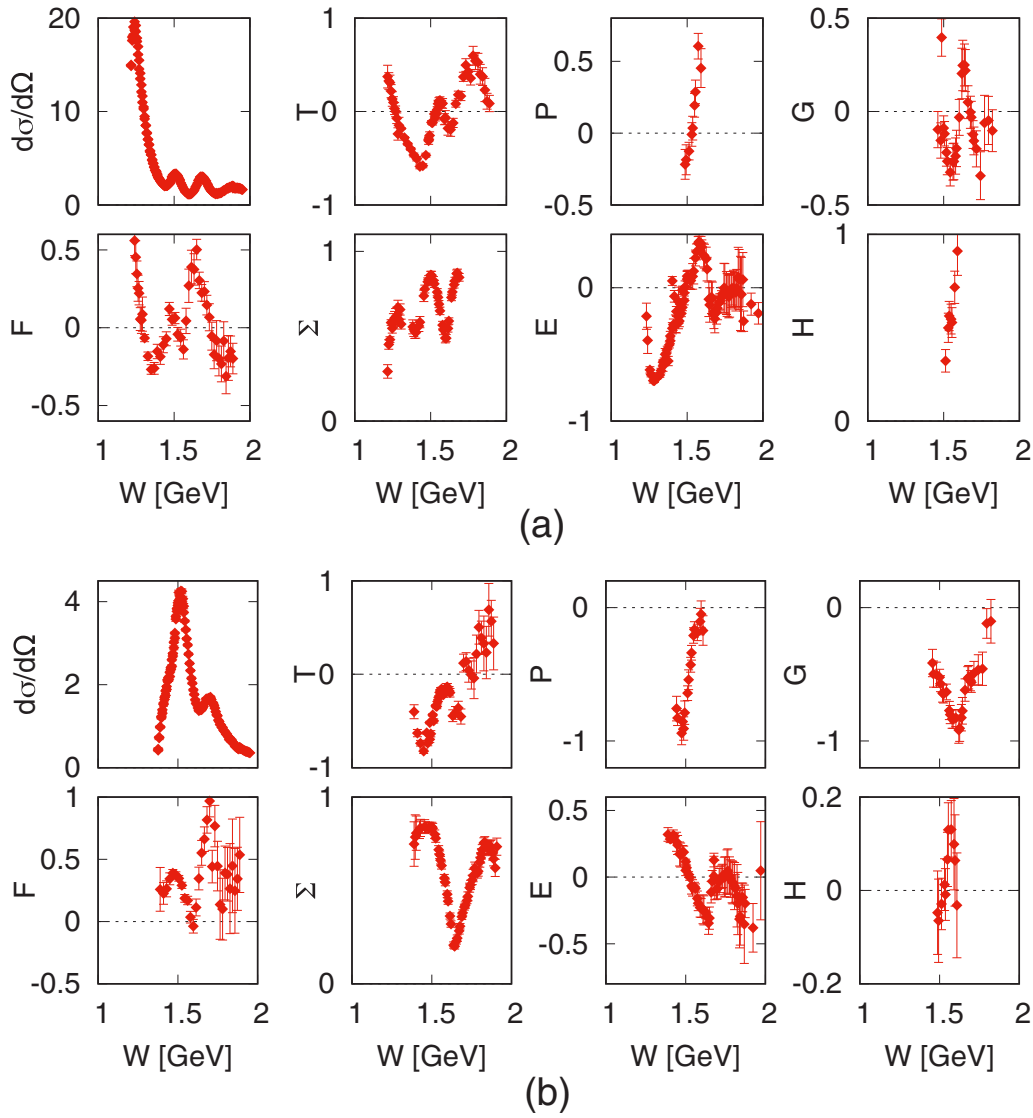

FIG. 2. Example of our interpolated fixed-t database. In (a), we give interpolated data for $t = -0.2$ GeV^2, and in (b), we give interpolated data for $t = -0.5$ GeV^2.

very small energy bins from 1 to 5 MeV depending on the beam energy. The polarization observables Σ, T, F, and E are also available at the full energy region ($W < 1.9$ GeV) and cover the most angular range, whereas the polarization observables G, P, and H were measured only in a limited energy range. A summary is given in Table I.

In general, there is a hierarchy of precision depending on the polarization degrees of freedom used in the experiment. The highest precision was achieved in measurements of the unpolarized differential cross section at MAMI [22]. The statistical uncertainties are so small that systematic uncertainties due to angular-dependent detection efficiencies had to be taken into account. For all other observables, the uncertainties in the angular distributions are dominated by statistics. Normalization errors (luminosity and polarization degree) are below 5% and are not taken into account in this analysis.

For our single-energy fits, we need all observables at the same values of $W = \sqrt{s}$ and for the fixed-t fits at the same values of t. Typically, this is not provided by the experiments directly. The data are given in bins of W and c.m. angle $\theta_{\rm cm}$ with bin sizes and central values varying between different data sets. Therefore, some interpolation between measurements at different energies and angles is necessary. We created energy bins of about 5–10 MeV width using a spline smoothing method [33] which was similarly applied in the Karlsruhe-Helsinki analysis KH80 [19] and in our previous analysis of η production [18]. The uncertainties of interpolated data points are taken to be equal to the errors of nearest measured data points. Our fixed-t amplitude analysis is performed at t values in the range of -1.00 GeV$^2 < t < -0.005$ GeV^2 with 20 equidistant t values. Examples of interpolated data points at $t = -0.2$ and -0.5 GeV^2 are shown in Fig. 2. We note that the individual errors are not independent.

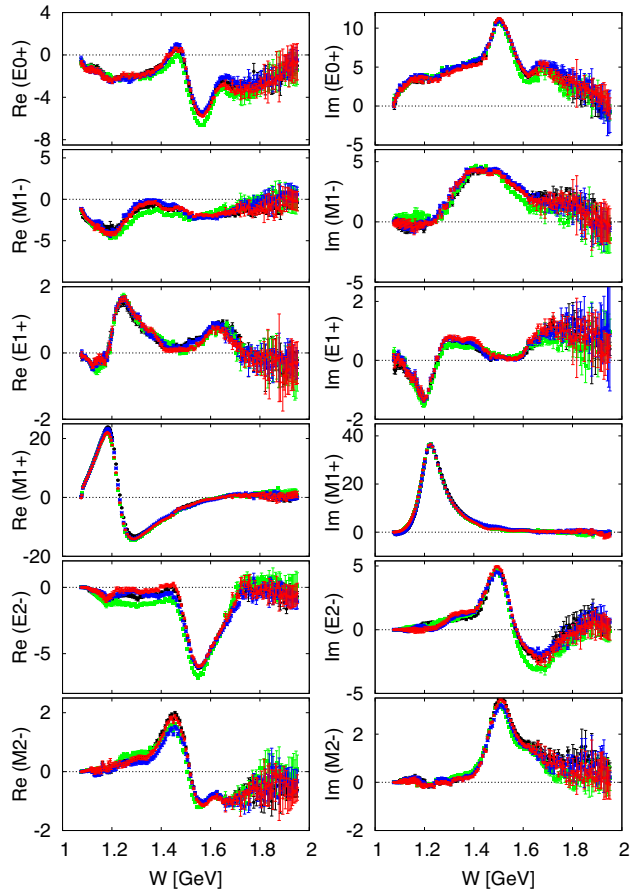

FIG. 3. SE1, …, SE4 solutions obtained using different models as initial solutions [BnGa (black circles), JüBo (blue asterisks), SAID (red diamonds), and MAID (green squares)], see the text for further details. Multipoles are in units of am (am ≡ mFm).

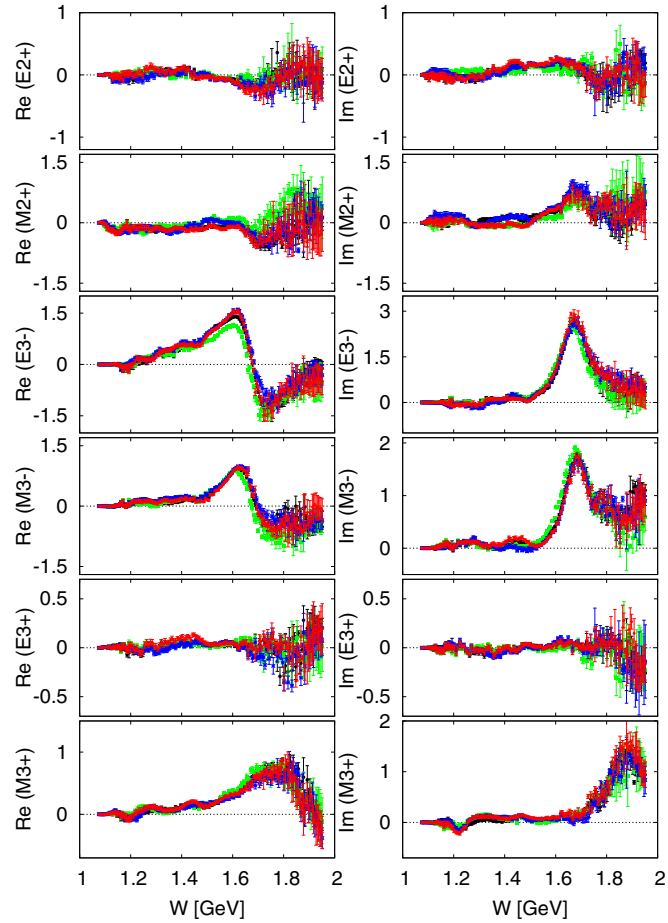

FIG. 4. SE1, …, SE4 solutions obtained using different models as initial solutions [BnGa (black circles), JüBo (blue asterisks), SAID (red diamonds), and MAID (green squares)], see the text for further details. Multipoles are in units of am (am ≡ mFm).

B. π^0 photoproduction multipoles

Fitting was performed in a standard way using the MINUIT program package, and the final result is presented in Figs. 3 and 4 where four different single-energy solutions are compared. For SE1, we use as a starting solution BG2014-02 from Bonn-Gatchina [1], for SE2, we use the JüBo2015-B solution from Jülich-Bonn [2], for SE3, we use the CM12 solution from SAID [3], and, for SE4, we use the MAID2007 solution from Mainz [4]. As can be seen from Table I, at energies of $W < 1.7$ GeV we use as much as eight observables σ_0, Σ, T, P, E, F, G, and H. However, as not all observables are taken at comparable energies, the maximum of five observables was fitted simultaneously (differential cross section + four spin observables). But the combination is not identical in each energy bin. At higher energies, the number of measured observables is reduced, so, at some energies, we use only two spin observables in addition to the cross section.

IV. DISCUSSION

In this paper, we use four different models BnGa [1], JüBo [2], SAID [3], and MAID [4] as initial solutions. We randomly scatter them with 30% uncertainty, and from these values, we generate four different SE solutions, SE1, …, SE4, which form a very well-defined band of solutions extending up to $W = 1.7$ GeV. In the remaining energy range of $1.7 < W < 1.9$ GeV, the four solutions do show some differences as we are going to discuss later on. Comparing Figs. 3 and 4, it may be seen that, in this energy range, our solutions demonstrate almost complete independence of initial solutions, despite the fact that some of them (Bonn-Gatchina, for instance) have very different E_0+ and M_1- multipoles in the energy range of 1.2 GeV $\leqslant W \leqslant$ 1.4 GeV (see Fig. 6).

Due to the fact that moderate changes in initial solutions do not cause large differences in final solutions, our method shows stability and robustness. In addition, our SE solutions are constrained by fixed-t analyticity. As we described in our previous work [18], our fixed-t constraint has a much deeper meaning than to ensure smoothness of our solution. The amplitudes in our method have a well-defined crossing symmetry and possess an analytic structure postulated by the Mandelstam hypothesis. Furthermore, it is expected that the multipoles obtained from those amplitudes also have an analytic structure as required by the Mandelstam hypothesis.

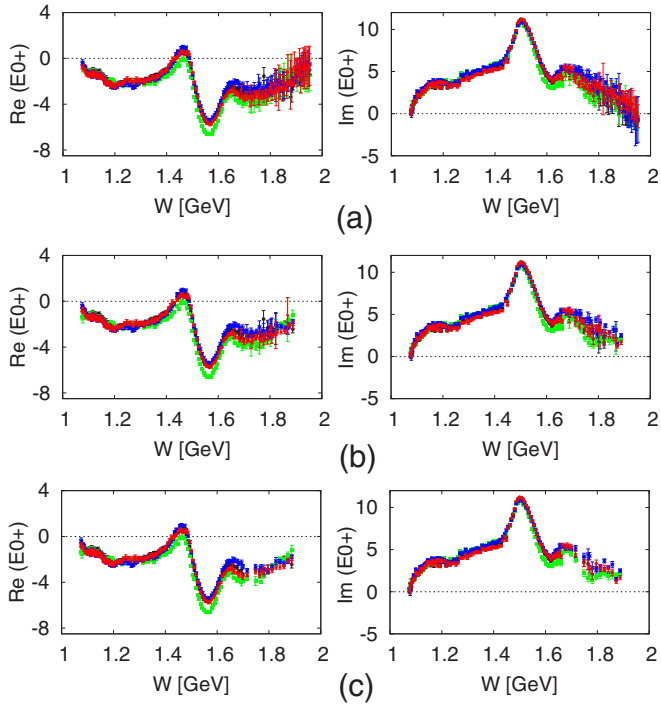

FIG. 5. $E0+$ SE solutions obtained using different models as initial solutions [BnGa (black circles), JüBo (blue asterisks), SAID (red diamonds), and MAID (green squares)] with a different number of observables at an energy of $W > 1.7$ GeV. In (a), we give the standard solution, in (b), we omit the energy points where only two observables are measured (three and more), and in (c), we omit the energy points where only three observables are measured (four and more). Multipoles are in units of am (am $\equiv$ mFm).

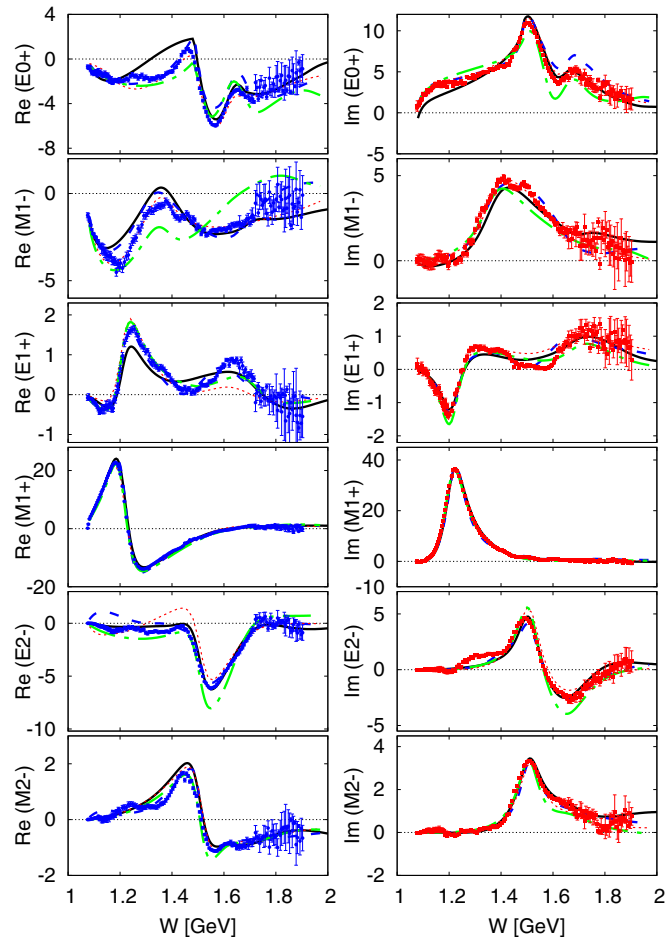

FIG. 6. Electric and magnetic multipoles from S_{11}, P_{11}, P_{13}, and D_{13} partial waves. Real and imaginary parts of the avarage SEav solution defined in the text (blue circles and red squares, respectively) and multipoles from models [BnGa (black full lines), JüBo (blue long-dashed lines), SAID (red short-dashed lines), and MAID2007 (green dashed-dotted lines)]. Multipoles are in units of am (am $\equiv$ mFm).

Our SE solutions start to become poorly determined at energies of $W > 1.7$ GeV. Solutions obtained from different initial solutions differ significantly and show large errors. This is due to the lack of experimental data, especially the lack of certain polarization observables as we will further outline in the following. The number of measured observables is much smaller. In addition, the constraining power of the fixed-t analyticity decreases, especially for large $-t$ values in the backward angular range. As can be seen in Fig. 12, the unphysical ν region for large $-t$ values increases strongly. As a consequence, the Pietarinen functions in the FT AA are less constrained by experimental data, and therefore, the SE solutions are less constrained by fixed-t analyticity [34].

Concerning the data, as can be seen from Table I, at energies of $W < 1.7$ GeV we use as much as eight observables σ_0, Σ, T, P, E, F, G, and H, fitting maximally five of them at the same time. However, at energies of $W > 1.7$ GeV, the number of measured observables becomes much smaller (not bigger than four, and often much less), and the partial-wave reconstruction must become less reliable. In Fig. 5, we give an indication of what happens with partial-wave reconstruction for the $E0+$ multipole when different numbers of measured observables are used in the fit. In Fig. 5(a), we give the solution for all energies and all measured observables, in Fig. 5(b) we omit the energy points where only two observables are measured (three and more), and in Fig. 5(c), we omit the energy points where only three observables are measured (four and more). It is obvious that error bars significantly drop as the number of observables grows. However, the error bars are still somewhat bigger than at lower energies, but this is entirely due to the quality of the measured data. So, improving the database at higher energies in the sense that both the number of observables and the quality of measurements are increased will improve the quality of the solution using the present technique.

We create the "averaged" solution by performing an average over the four SE solutions SE1, …,SE4 and taking this solution as input for the first iteration in the final fitting procedure.

The result for this particular solution is shown in Figs. 6 and 7 where it is also compared with all four ED solutions. The averaged SE (SEav) solution agrees fairly well with all ED solutions. As could be expected, the SEav solution actually follows the average line of ED solutions. However,

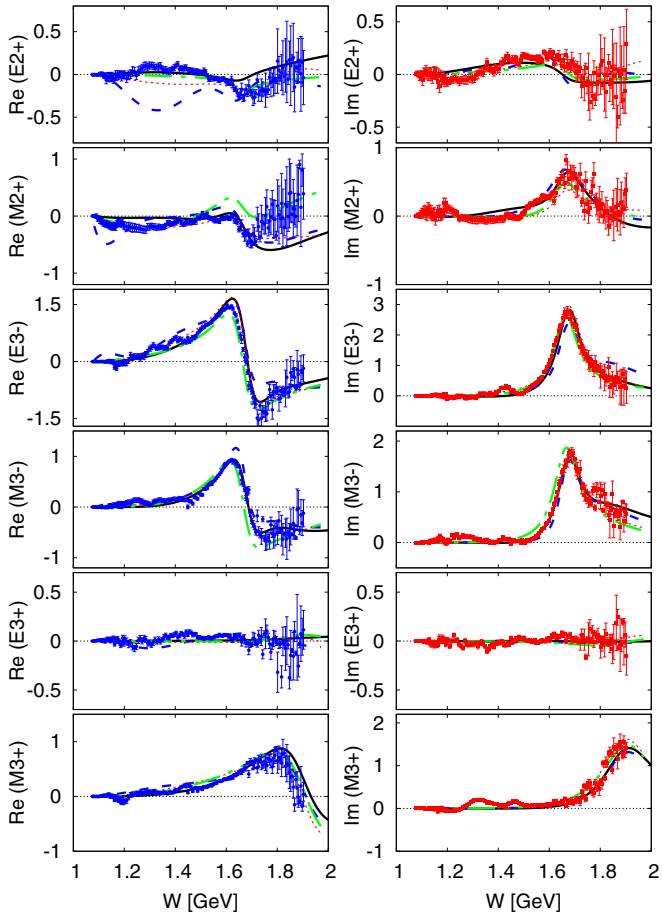

FIG. 7. Electric and magnetic multipoles from D_{15}, F_{15}, and F_{17} partial waves. Real and imaginary parts of the avarage SEav solution defined in the text (blue circles and red squares, respectively) and multipoles from models [BnGa (black full lines), JüBo (blue long-dashed lines), SAID (red short-dashed lines), and MAID2007 (green dashed-dotted lines)]. Multipoles are in units of am (am ≡ mFm).

there are some bigger variations in the energy range of $1.2 < W < 1.4$ GeV.

Next, we will discuss what could be improved in the present database in order to obtain SE solutions that all converge to a single one. Despite the abundance of experimental data in pion photoproduction and especially for $p(\gamma,\pi^0)p$, we know that the complete set of observables needed for a unique amplitude reconstruction has still not been measured. As we see in Table I, a total of eight observables at various energies has already been measured. Four of them (σ_0, Σ, T, and P) belong to the single-spin type ($\mathcal{S}$), and the remaining four (E, F, G, and H) belong to the beam-target type ($\mathcal{BT}$). However, for a complete amplitude experiment, also two recoil observables out of the groups ($O_{x'}, O_{z'}, C_{x'}, C_{z'}$) of beam-recoil type and ($T_{x'}, T_{z'}, L_{x'}, L_{z'}$) of target-recoil type ($\mathcal{TR}$). For pion and η photoproductions, such experiments are extremely difficult as a recoil polarimetry has to be applied for the outgoing nucleon [see Ref. [35]. In a pilot experiment at MAMI, this has been performed for ($\mathcal{BR}$)-type observables. However, for a PWA, these first data points are too scarce and have large uncertainties. In the following, we ignore $\mathcal{TR}$-type observables, which are even more difficult to measure.

In Figs. 8–11, we show the results of the fit of all four SE solutions and the averaged SEav solution with the measured data and predictions for a number of unmeasured observables at four representative energies $W = 1.201,\ 1.481,\ 1.660$, and 1.872 GeV. Figures 8–11(a) show the comparison of the averaged SEav solution with the measured database at chosen energies, and it turns out that the four SE1, …,SE4 solutions as well as the avaraged SEav solution give practically identical results. Figures 8–11(b) show the predictions of our five SE1, …,SEav solutions for unmeasured observables which together with the measured ones can form several complete sets of observables. Different conclusions emerge for different energies.

At the lowest energy of $W = 1.201$ GeV, we have four measured observables, and the measured data are of good quality. The fit is almost perfect. Next, we show the eight unmeasured observables out of the groups $\mathcal{S}$, $\mathcal{BT}$, and $\mathcal{BR}$ predicted from our four SE1, …,SE4 solutions. We can see that the agreement of all four predictions for all observables is fairly good with the exception of P, G, and H observables. The differences are rather small, so only a small improvement in a PWA can be expected.

At the energy of $W = 1.481$ GeV, we have five measured observables, and the measured data are of good quality. The fit is almost perfect. Next, we show the seven unmeasured observables out of the groups $\mathcal{S}$, $\mathcal{BT}$, and $\mathcal{BR}$ predicted from our four SE1, …,SE4 solutions. We see that the agreement of all four predictions for all observables is fairly good with the exception of $O_{x'}$, $O_{z'}$, and $C_{x'}$ observables. The differences are rather small, so only a little improvement is expected.

At the energy of $W = 1.660$ GeV, we have four measured observables, and the measured data are still of good quality. The fit is almost perfect. Next, we show the eight unmeasured observables out of the groups $\mathcal{S}$, $\mathcal{BT}$, and $\mathcal{BR}$ predicted from our four SE1, …,SE4 solutions. We can now see a spread for all observables at this and higher energies. The agreement is acceptable for $C_{x'}$, $C_{z'}$, $O_{x'}$, and $O_{z'}$, whereas it is notably worse for F, H, T, and P. So, we expect some improvement in the uniqueness of the SE PWA if these observables are more precisely measured. We recommend to remeasure the configuration T, P, $C_{x'}$, and $O_{z'}$ as the predictions for the beam-recoil observables are fairly similar, whereas one must only remeasure simpler single-spin observables T and P.

At the highest energy of $W = 1.872$ GeV, we have five measured observables where four of them have an acceptable quality, only the F observable is more uncertain. The fit is almost perfect. Next, we show the seven unmeasured observables out of the groups $\mathcal{S}$, $\mathcal{BT}$, and $\mathcal{BR}$ predicted from our four SE1, …,SE4 solutions. We see that the agreement of all four predictions for all observables is not good for either of them.

V. SUMMARY AND CONCLUSIONS

Using the formalism introduced and explained for η photoproduction in Ref. [18], we have performed a fixed-t single-energy partial-wave analysis of π^0 photoproduction on the world collection of data.

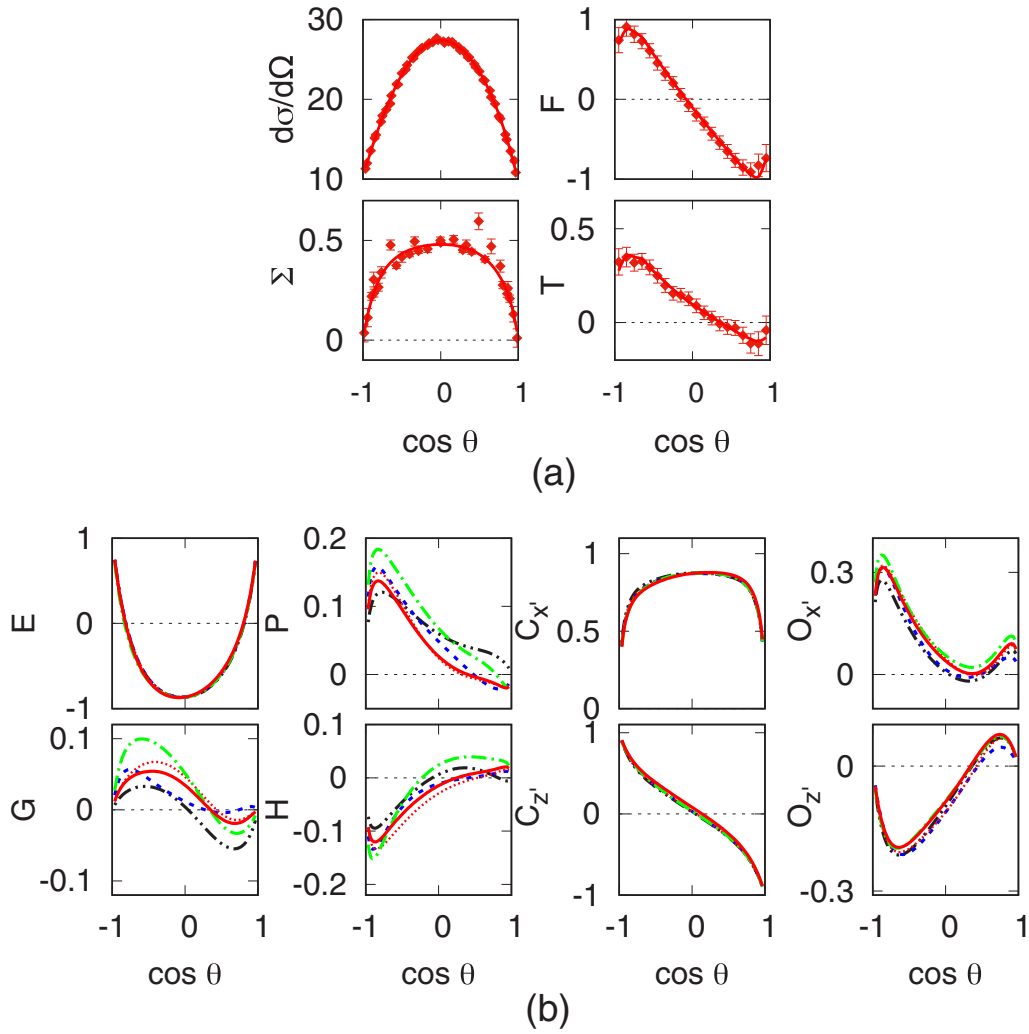

FIG. 8. In (a), the single-energy fit SEav compared to the experimental data with four observables at $E = 0.3$ ($W = 1.201$ GeV). In (b), predictions from five different single-energy solutions, SE1 (black dot-dot-dashed line), SE2 (blue short-dashed line), SE3 (red dotted line), SE4 (green dashed-dotted line), and SEav (solid red line) for polarization observables that are not fitted $\{E, P, C_{x'}, O_{x'}\}$ (top) and $\{G, H, C_{z'}, O_{z'}\}$ (bottom) at an energy of $E = 0.3$ ($W = 1.201$ GeV).

In an iterative two-step process, the single-energy multipoles are constrained by fixed-t Pietarinen expansions fitted to experimental data. This leads to a partial-wave expansion that obeys fixed-t analyticity with a least model dependence.

In the energy range of $E = 0.14 - 1.46$ ($W =$ 1.08–1.9 GeV), we have obtained electric and magnetic multipoles $E_{\ell\pm}, M_{\ell\pm}$, up to F waves, $\ell = 3$ in 158 energy bins of about 5–10-MeV width. First, we used randomized starting solutions from BnGa, JüBo, SAID, and MAID energy-dependent solutions and obtained four different SE solutions, SE1, …,SE4 in an iterative procedure. These four SE solutions appeared already much closer together than the four underlying ED solutions where we started from. Second, we generated an average SE solution, SEav, again in an iterative process. All five SE solutions compare very well with the experimental data where the averaged solution SEav is obtained in the least model-dependent way.

Finally, we compared our five SE solutions in their predictions for unmeasured polarization observables. At lower energies, the spread of these predictions is rather small, but it becomes quite large at higher energies where it will help to propose new measurements in order to get a unique PWA.

ACKNOWLEDGMENTS

This work was supported by the Deutsche Forschungsgemeinschaft (Grant No. SFB 1044).

APPENDIX A: KINEMATICS IN π^0 PHOTOPRODUCTION

For π photoproduction on the nucleon, we consider the reaction,

$$\gamma(k) + N(p_i) \to \pi(q) + N'(p_f), \tag{A1}$$

where the variables in brackets denote the four-momenta of the participating particles. In the pion-nucleon c.m. system,

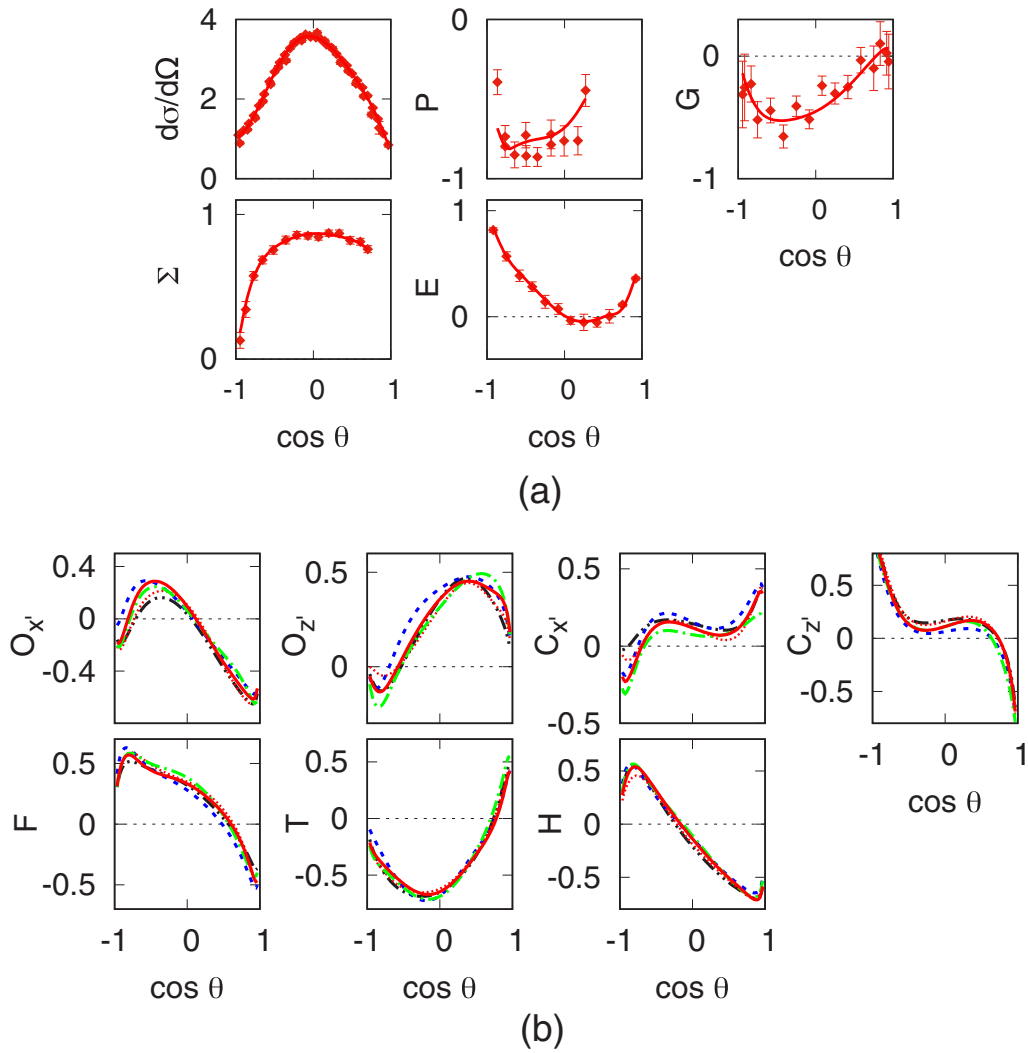

FIG. 9. In (a), the single-energy fit SEav compared to the experimental data with five observables at $E = 0.7$ ($W = 1.481$ GeV). In (b), predictions from five different single-energy solutions, SE1 (black dot-dot-dashed line), SE2 (blue short-dashed line), SE3 (red dotted line), SE4 (green dashed-dotted line), and SEav (solid red line) for polarization observables that are not fitted $\{O_{x'}, O_{z'}, C_{x'}, C_{z'}\}$ (top) and $\{F, T, H\}$ (bottom) at an energy of $E = 0.7$ ($W = 1.481$ GeV).

we define

$$k^\mu = (\omega_\gamma, \mathbf{k}), \quad q^\mu = (\omega_\pi, \mathbf{q}) \tag{A2}$$

for a photon and pion meson, and

$$p_i^\mu = (E_i, \mathbf{p}_i), \quad p_f^\mu = (E_f, \mathbf{p}_f) \tag{A3}$$

for incoming and outgoing nucleons, respectively. The familiar Mandelstam variables are given as

$$s = W^2 = (p_i + k)^2, \quad t = (q - k)^2, \quad u = (p_f - q)^2, \tag{A4}$$

the sum of the Mandelstam variables is given by the sum of the external masses,

$$s + t + u = 2m_N^2 + m_\pi^2, \tag{A5}$$

where m_N and m_π are masses of the proton and π meson, respectively. In the pion-nucleon c.m. system, the energies and momenta can be related to the Mandelstam variable s by

$$k = |\mathbf{k}| = \frac{s - m_N^2}{2\sqrt{s}}, \quad \omega = \frac{s + m_\pi^2 - m_N^2}{2\sqrt{s}}, \tag{A6}$$

$$q = |\mathbf{q}| = \left[\left(\frac{s - m_\pi^2 + m_N^2}{2\sqrt{s}}\right) - m_N^2\right]^{1/2}, \tag{A7}$$

$$E_i = \frac{s - m_N^2}{2\sqrt{s}}, \quad E_f = \frac{s + m_N^2 + m_\pi^2}{2\sqrt{s}}, \tag{A8}$$

$W = \sqrt{s}$ is the c.m. energy. Furthermore, we will also refer to the laboratory energy of the photon $E = (s - m_N^2)/(2m_N)$.

Starting from the s-channel reaction $\gamma + N \Rightarrow \pi + N$ using a crossing relation, one obtains two other channels,

$$\gamma + \pi \quad \Rightarrow \quad N + \bar{N}, \quad t \text{ channel}, \tag{A9}$$

$$\pi + \bar{N} \quad \Rightarrow \quad \gamma + \bar{N}, \quad u \text{ channel}. \tag{A10}$$

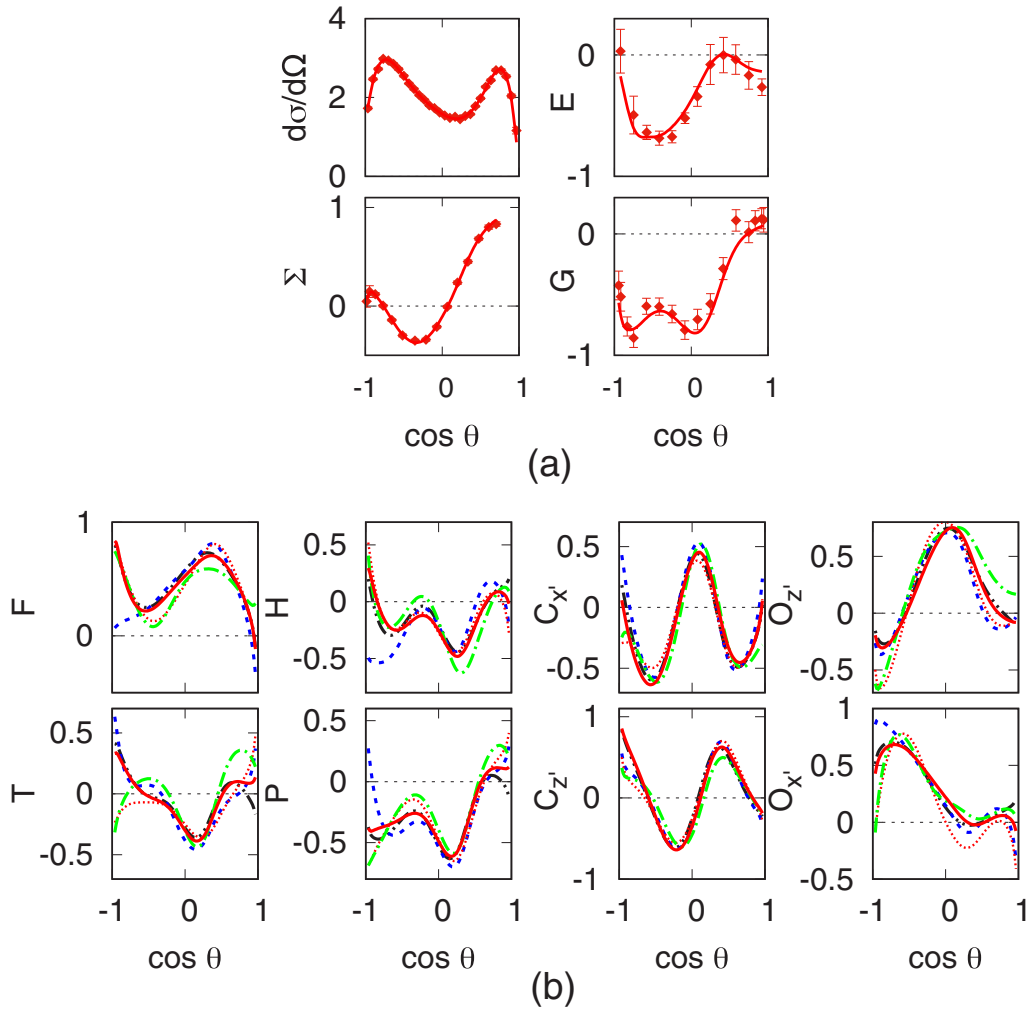

FIG. 10. In (a), the single-energy fit SEav compared to the experimental data with four observables at $E = 1.0$ ($W = 1.660$ GeV). In (b), predictions from five different single-energy solutions, SE1 (black dot-dot-dashed line), SE2 (blue short-dashed line), SE3 (red dotted line), SE4 (green dashed-dotted line), and SEav (solid red line) for polarization observables that are not fitted $\{F, H, C_{x'}, O_{z'}\}$ (top) and $\{T, P, C_{z'}, O_{x'}\}$ (bottom) at an energy of $E = 1.0$ ($W = 1.660$ GeV).

All three channels defined above are described by a set of four invariant amplitudes. The singularities of the invariant amplitudes are defined by unitarity in s, u, and t channels,

$$s\text{-channel cut: } (m_N + m_\pi)^2 \leqslant s < \infty, \tag{A11}$$

$$u\text{-channel cut: } (m_N + m_\pi)^2 \leqslant u < \infty, \tag{A12}$$

and nucleon poles at $s = m_N^2$, $u = m_N^2$. The crossing symmetrical variable is

$$\nu = \frac{s - u}{4m_N}. \tag{A13}$$

The s-channel region is shown in Fig. 12. The upper and lower boundaries of the physical region are given by the scattering angles $\theta = 0$ and $\theta = 180^\circ$, respectively. The c.m. energy W and the c.m. scattering angle θ can be obtained from the variables ν and t by

$$W^2 = m_N(m_N + 2\nu) - \tfrac{1}{2}\left(t - m_\pi^2\right), \tag{A14}$$

and

$$\cos\theta = \frac{t - m_\pi^2 + 2k\omega}{2kq}. \tag{A15}$$

APPENDIX B: CROSS SECTION AND POLARIZATION OBSERVABLES

Experiments with three types of polarization can be performed in meson photoproduction: photon beam polarization, polarization of the target nucleon, and polarization of the recoil nucleon. Target polarization will be described in the frame $\{x, y, z\}$ in Fig. 13 with the z axis pointing into the direction of the photon momentum $\hat{\mathbf{k}}$, the y axis perpendicular to the reaction plane $\hat{\mathbf{y}} = \hat{\mathbf{k}} \times \hat{\mathbf{q}}/\sin\theta$, and the x axis given by $\hat{\mathbf{x}} = \hat{\mathbf{y}} \times \hat{\mathbf{z}}$. For recoil polarization, we will use the frame $\{x', y', z'\}$ with the z' axis defined by the momentum vector of the outgoing meson $\hat{\mathbf{q}}$, the y' axis as for target polarization, and the x' axis given by $\hat{\mathbf{x}}' = \hat{\mathbf{y}}' \times \hat{\mathbf{z}}'$.

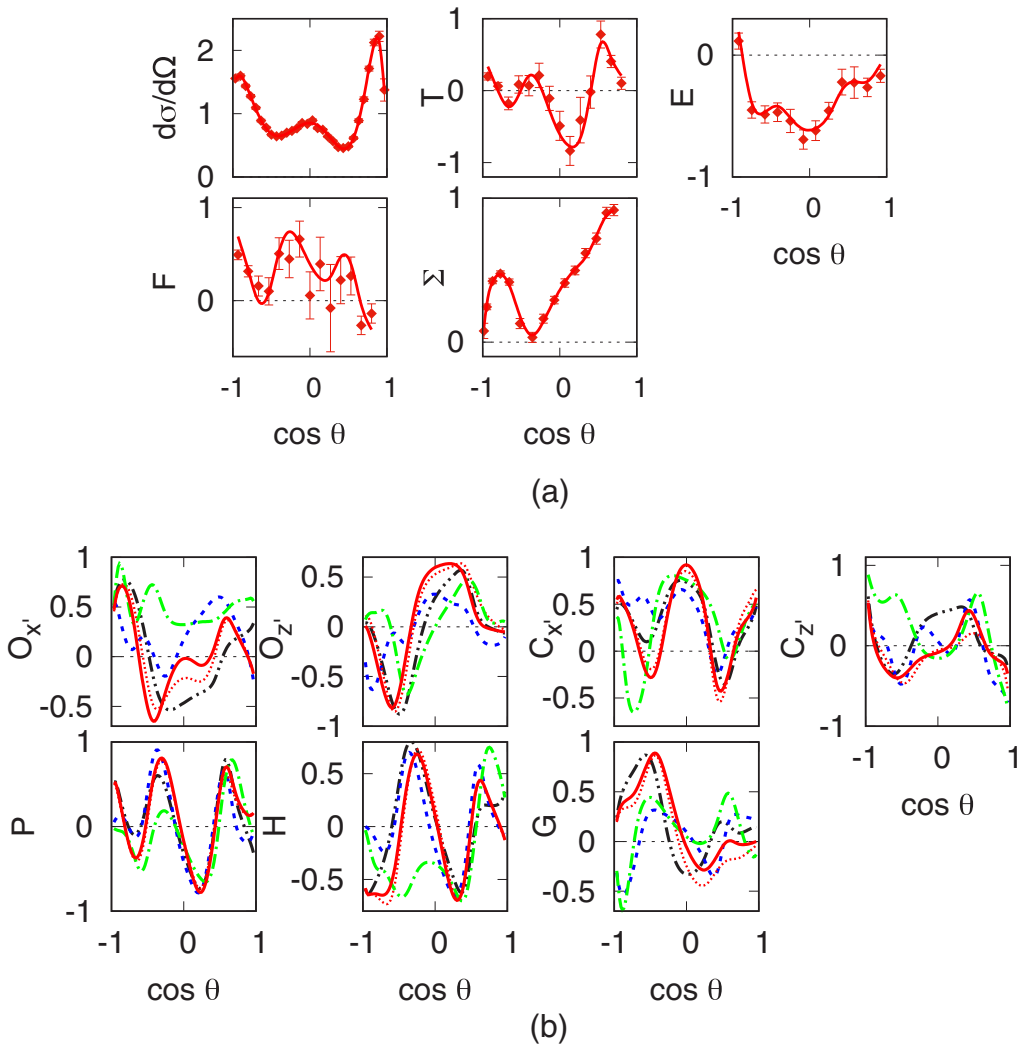

FIG. 11. In (a), the single-energy fit SEav compared to the experimental data with five observables at $E = 1.4$ ($W = 1.852$ GeV). In (b), predictions from five different single-energy solutions, SE1 (black dot-dot-dashed line), SE2 (blue short-dashed line), SE3 (red dotted line), SE4 (green dashed-dotted line), and SEav (solid red line) for polarization observables that are not fitted $\{O_{x'}, O_{z'}, C_{x'}, C_{z'}\}$ (top) and $\{P, H, G\}$ (bottom) at an energy of $E = 1.4$ ($W = 1.872$ GeV).

The photon polarization can be linear or circular. For a linear photon polarization ($P_T = 1$) on the reaction plane $\hat{\mathbf{x}}$, we get $\varphi = 0$ and perpendicular in direction $\hat{\mathbf{y}}$, and the polarization angle is $\varphi = \pi/2$. For right-handed circular polarization, $P_\odot = +1$.

We may classify the differential cross sections by the three classes of double polarization experiments and one class of triple polarization experiments, which, however, do not give additional information:

(1) polarized photons and polarized target,

$$\frac{d\sigma}{d\Omega} = \sigma_0\{1 - P_T\Sigma\ \cos\ 2\varphi + P_x(-P_T H\ \sin\ 2\varphi + P_\odot F) + P_y(T - P_T P\ \cos\ 2\varphi) + P_z(P_T G\ \sin\ 2\varphi - P_\odot E)\}, \tag{B1}$$

(2) polarized photons and recoil polarization,

$$\frac{d\sigma}{d\Omega} = \sigma_0\{1 - P_T\Sigma\ \cos\ 2\varphi + P_{x'}(-P_T O_{x'}\ \sin\ 2\varphi - P_\odot C_{x'}) + P_{y'}(P - P_T T\ \cos\ 2\varphi) + P_{z'}(-P_T O_{z'}\ \sin\ 2\varphi - P_\odot C_{z'})\}, \tag{B2}$$

(3) polarized target and recoil polarization,

$$\frac{d\sigma}{d\Omega} = \sigma_0\{1 + P_y T + P_{y'} P + P_{x'}(P_x T_{x'} - P_z L_{x'}) + P_{y'} P_y \Sigma + P_{z'}(P_x T_{z'} + P_z L_{z'})\}. \tag{B3}$$

In these equations, σ_0 denotes the unpolarized differential cross section, the transverse degree of photon polarization is denoted by P_T, $P_\odot$ is the right-handed circular photon polarization, and φ is the azimuthal angle of the photon polarization vector with respect to the reaction plane. Instead of

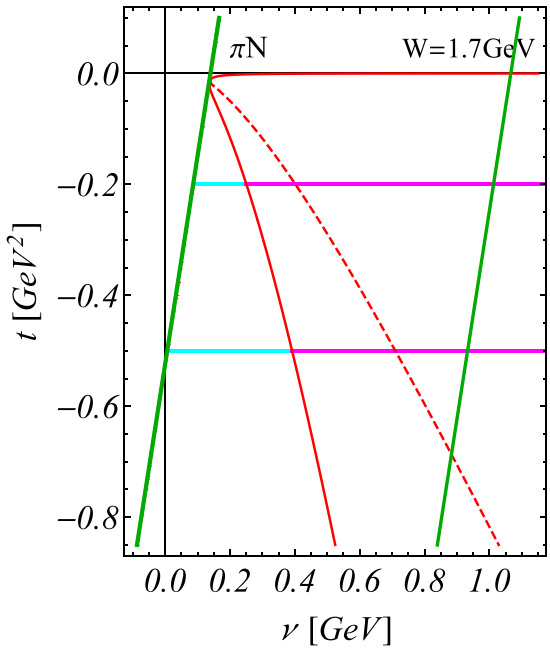

FIG. 12. The Mandelstam plane for pion photoproduction on the nucleon. The red solid curves are the boundaries of the physical region from $\theta = 0$ to $\theta = 180^\circ$ and the red dashed line shows $\theta = 90^\circ$. The green tilted vertical lines are the threshold for pion production at $W = 1.073$ and $W = 1.7$ GeV. The horizontal lines denote the t-values $-0.2, -0.5$ GeV^2. The magenta parts give the part inside the physical region, whereas the cyan parts indicate nonzero amplitudes in the unphysical region. The fixed-t threshold values for γ, π in W are $W_{\rm thr} = 1.208$ ($t = -0.2$ GeV^2) and $W_{\rm thr} = 1.369$ ($t = -0.5$ GeV^2).

asymmetries, in the following, we will often discuss the product of the unpolarized cross section with the asymmetries and will use the notation $\check{\Sigma} = \sigma_0\Sigma$, $\check{T} = \sigma_0 T, \ldots$. In Appendix C, we give expressions of the observables in terms of CGLN and helicity amplitudes.

APPENDIX C: OBSERVABLES EXPRESSED IN CGLN AND HELICITY AMPLITUDES

Spin observables expressed in CGLN amplitudes are given by

$$\sigma_0 = \mathrm{Re}\{F_1^*F_1 + F_2^*F_2 + \sin^2\theta(F_3^*F_3/2 + F_4^*F_4/2 + F_2^*F_3 + F_1^*F_4 + \cos\theta F_3^*F_4) - 2\cos\theta F_1^*F_2\}\rho, \quad \text{(C1)}$$

$$\check{\Sigma} = -\sin^2\theta\,\mathrm{Re}\{F_3^*F_3 + F_4^*F_4)/2 + F_2^*F_3 + F_1^*F_4 + \cos\theta F_3^*F_4\}\rho, \quad \text{(C2)}$$

$$\check{T} = \sin\theta\,\mathrm{Im}\{F_1^*F_3 - F_2^*F_4 + \cos\theta(F_1^*F_4 - F_2^*F_3) - \sin^2\theta F_3^*F_4\}\rho, \quad \text{(C3)}$$

$$\check{P} = -\sin\theta\,\mathrm{Im}\{2F_1^*F_2 + F_1^*F_3 - F_2^*F_4 - \cos\theta(F_2^*F_3 - F_1^*F_4) - \sin^2\theta F_3^*F_4\}\rho, \quad \text{(C4)}$$

$$\check{E} = \mathrm{Re}\{F_1^*F_1 + F_2^*F_2 - 2\cos\theta F_1^*F_2 + \sin^2\theta(F_2^*F_3 + F_1^*F_4)\}\rho, \quad \text{(C5)}$$

$$\check{F} = \sin\theta\,\mathrm{Re}\{F_1^*F_3 - F_2^*F_4 - \cos\theta(F_2^*F_3 - F_1^*F_4)\}\rho, \quad \text{(C6)}$$

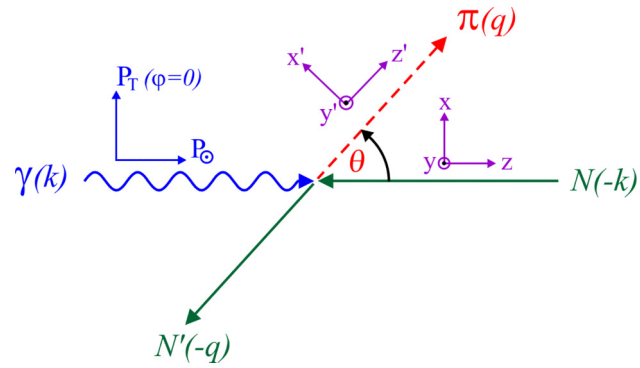

FIG. 13. Kinematics of photoproduction and frames for polarization. The frame $\{x, y, z\}$ is used for target polarization $\{P_x, P_y, P_z\}$, whereas the recoil polarization $\{P_{x'}, P_{y'}, P_{z'}\}$ is defined in the frame $\{x', y', z'\}$, which is rotated around $y' = y$ by the polar angle θ. The azimuthal angle φ is defined on the $\{x, y\}$ plane and is zero in the projection shown in the figure.

$$\check{G} = \sin^2\theta\,\mathrm{Im}\{F_2^*F_3 + F_1^*F_4\}\rho, \quad \text{(C7)}$$

$$\check{H} = \sin\theta\,\mathrm{Im}\{2F_1^*F_2 + F_1^*F_3 - F_2^*F_4 + \cos\theta(F_1^*F_4 - F_2^*F_3)\}\rho, \quad \text{(C8)}$$

$$\check{C}_{x'} = \sin\theta\,\mathrm{Re}\{F_1^*F_1 - F_2^*F_2 - F_2^*F_3 + F_1^*F_4 - \cos\theta(F_2^*F_4 - F_1^*F_3)\}\rho, \quad \text{(C9)}$$

$$\check{C}_{z'} = \mathrm{Re}\{2F_1^*F_2 - \cos\theta(F_1^*F_1 + F_2^*F_2) + \sin^2\theta(F_1^*F_3 + F_2^*F_4)\}\rho, \quad \text{(C10)}$$

$$\check{O}_{x'} = \sin\theta\,\mathrm{Im}\{F_2^*F_3 - F_1^*F_4 + \cos\theta(F_2^*F_4 - F_1^*F_3)\}\rho, \quad \text{(C11)}$$

$$\check{O}_{z'} = -\sin^2\theta\,\mathrm{Im}\{F_1^*F_3 + F_2^*F_4\}\rho, \quad \text{(C12)}$$

TABLE II. Spin observables expressed by helicity amplitudes in the notation of Barker [36] and Walker [37]. A phase-space factor q/k has been omitted in all expressions. The differential cross section is given by σ_0, and the spin observables $\check{O}_i$ are obtained from the spin asymmetries A_i by $\check{O}_i = A_i\sigma_0$.

Observable	Helicity representation	Type
σ_0	$\frac{1}{2}(\lvert H_1\rvert^2 + \lvert H_2\rvert^2 + \lvert H_3\rvert^2 + \lvert H_4\rvert^2)$	
$\check{\Sigma}$	$\mathrm{Re}(H_1H_4^* - H_2H_3^*)$	$\mathcal{S}$
$\check{T}$	$\mathrm{Im}(H_1H_2^* + H_3H_4^*)$	(Single spin)
$\check{P}$	$-\mathrm{Im}(H_1H_3^* + H_2H_4^*)$	
$\check{G}$	$-\mathrm{Im}(H_1H_4^* + H_2H_3^*)$	
$\check{H}$	$-\mathrm{Im}(H_1H_3^* - H_2H_4^*)$	$\mathcal{BT}$
$\check{E}$	$\frac{1}{2}(-\lvert H_1\rvert^2 + \lvert H_2\rvert^2 - \lvert H_3\rvert^2 + \lvert H_4\rvert^2)$	(Beam target)
$\check{F}$	$\mathrm{Re}(H_1H_2^* + H_3H_4^*)$	
$\check{O}_{x'}$	$-\mathrm{Im}(H_1H_2^* - H_3H_4^*)$	
$\check{O}_{z'}$	$\mathrm{Im}(H_1H_4^* - H_2H_3^*)$	$\mathcal{BR}$
$\check{C}_{x'}$	$-\mathrm{Re}(H_1H_3^* + H_2H_4^*)$	(Beam recoil)
$\check{C}_{z'}$	$\frac{1}{2}(-\lvert H_1\rvert^2 - \lvert H_2\rvert^2 + \lvert H_3\rvert^2 + \lvert H_4\rvert^2)$	
$\check{T}_{x'}$	$\mathrm{Re}(H_1H_4^* + H_2H_3^*)$	
$\check{T}_{z'}$	$\mathrm{Re}(H_1H_2^* - H_3H_4^*)$	$\mathcal{TR}$
$\check{L}_{x'}$	$-\mathrm{Re}(H_1H_3^* - H_2H_4^*)$	(Target recoil)
$\check{L}_{z'}$	$\frac{1}{2}(\lvert H_1\rvert^2 - \lvert H_2\rvert^2 - \lvert H_3\rvert^2 + \lvert H_4\rvert^2)$	

$$\check{L}_{x'} = -\sin\theta\,\mathrm{Re}\{F_1^*F_1 - F_2^*F_2 - F_2^*F_3 + F_1^*F_4 + \sin^2\theta (F_4^*F_4 - F_3^*F_3)/2 + \cos\theta(F_1^*F_3 - F_2^*F_4)\}\rho, \quad \text{(C13)}$$

$$\check{L}_{z'} = \mathrm{Re}\{2F_1^*F_2 - \cos\theta(F_1^*F_1 + F_2^*F_2) + \sin^2\theta(F_1^*F_3 + F_2^*F_4 + F_3^*F_4) + \cos\theta\,\sin^2\theta(F_3^*F_3 + F_4^*F_4)/2\}\rho, \quad \text{(C14)}$$

$$\check{T}_{x'} = -\sin^2\theta\,\mathrm{Re}\{F_1^*F_3 + F_2^*F_4 + F_3^*F_4 + \cos\theta(F_3^*F_3 + F_4^*F_4)/2\}\rho, \quad \text{(C15)}$$

$$\check{T}_{z'} = \sin\theta\,\mathrm{Re}\{F_1^*F_4 - F_2^*F_3 + \cos\theta(F_1^*F_3 - F_2^*F_4) + \sin^2\theta(F_4^*F_4 - F_3^*F_3)/2\}\rho, \quad \text{(C16)}$$

$$\text{with } \check{\Sigma} = \Sigma\sigma_0 \text{ etc., and } \rho = q/k. \quad \text{(C17)}$$

The 16 polarization observables of pseudoscalar photoproduction fall into four groups, single spin with unpolarized cross section included, beam-target, beam-recoil, and target-recoil observables. The simplest representation of these observables is given in terms of helicity amplitudes (see Table II).

[1] A. V. Anisovich *et al.*, Phys. Rev. C **96**, 055202 (2017); and references therein; and http://pwa.hiskp.uni-bonn.de/

[2] D. Rönchen, M. Döring, H. Haberzettl, J. Haidenbauer, U.-G. Meißner, and K. Nakayama, Eur. Phys. J. A **51**, 70 (2015); and references therein; and http://collaborations.fz-juelich.de/ikp/meson-baryon/main

[3] R. L. Workman, R. A. Arndt, W. J. Briscoe, M. W. Paris, and I. I. Strakovsky, Phys. Rev. C **86**, 035202 (2012); and http://gwdac.phys.gwu.edu/

[4] D. Drechsel, S. S. Kamalov, and L. Tiator, Eur. Phys. J. A **34**, 69 (2007); and https://maid.kph.uni-mainz.de/

[5] A. V. Anisovich *et al.*, Eur. Phys. J. A **52**, 284 (2016).

[6] A. S. Omelaenko, Yad. Fiz. **34**, 730 (1981).

[7] Y. Wunderlich, A. Švarc, R. L. Workman, L. Tiator, and R. Beck, Phys. Rev. C **96**, 065202 (2017).

[8] R. L. Workman, L. Tiator, Y. Wunderlich, M. Döring, and H. Haberzettl, Phys. Rev. C **95**, 015206 (2017).

[9] A. Švarc, Y. Wunderlich, H. Osmanović, M. Hadžimehmedović, R. Omerović, J. Stahov, V. Kashevarov, K. Nikonov, M. Ostrick, L. Tiator, and R. Workman, Phys. Rev. C **97**, 054611 (2018).

[10] A. B. Migdal, Sov. Phys. JETP **1**, 2 (1955).

[11] K. M. Watson, Phys. Rev. **88**, 1163 (1952).

[12] R. Beck *et al.*, Phys. Rev. C **61**, 035204 (2000).

[13] D. Hornidge *et al.* (A2 and CB-TAPS Collaborations), Phys. Rev. Lett. **111**, 062004 (2013).

[14] L. Markou, E. Stiliaris, and C. N. Papanicolas, Eur. Phys. J. A **54**, 115 (2018).

[15] G. Y. Chen, S. S. Kamalov, S. N. Yang, D. Drechsel, and L. Tiator, Phys. Rev. C **76**, 035206 (2007); L. Tiator, S. S. Kamalov, S. Ceci, G. Y. Chen, D. Drechsel, A. Svarc, and S. N. Yang, *ibid.* **82**, 055203 (2010).

[16] R. A. Arndt, W. J. Briscoe, I. I. Strakovsky, and R. L. Workman, Phys. Rev. C **74**, 045205 (2006).

[17] B. C. Hunt and D. M. Manley, Phys. Rev. C **99**, 055203 (2019); **99**, 055205 (2019).

[18] H. Osmanović, M. Hadžimehmedović, R. Omerović, J. Stahov, V. Kashevarov, K. Nikonov, M. Ostrick, L. Tiator, and A. Švarc, Phys. Rev. C **97**, 015207 (2018).

[19] G. Höhler, *Pion Nucleon Scattering*, Part 2, Landolt-Börnstein: Elastic and Charge Exchange Scattering of Elementary Particles Vol. 9b (Springer-Verlag, Berlin, 1983).

[20] E. Pietarinen, Nuovo Cimento Soc. Ital. Fis. **12A**, 522 (1972).

[21] J. Hamilton and J. L. Petersen, *New Development in Dispersion Theory* (Nordita, Copenhagen, 1973), Vol. 1.

[22] P. Adlarson *et al.* (A2 Collaboration at MAMI), Phys. Rev. C **92**, 024617 (2015).

[23] R. Beck, Eur. Phys. J. A **28**, 173 (2006).

[24] J. R. M. Annand *et al.* (A2 Collaboration at MAMI), Phys. Rev. C **93**, 055209 (2016).

[25] S. Schumann, B. P. Otte *et al.*, Phys. Lett. B **750**, 252 (2015); B. P. Otte, Ph.D. thesis, Mainz University, 2015.

[26] J. Linturi, Ph.D. thesis, Mainz University, 2015; F. Afzal, Ph.D. thesis. University of Bonn, (unpublished). We thank the A2 Collaboration at MAMI for providing data prior to the final publication.

[27] J. Ahrens *et al.*, Eur. Phys. J. A **26**, 135 (2005).

[28] J. Hartmann (CBELSA/TAPS Collaboration), Phys. Rev. Lett. **113**, 062001 (2014).

[29] M. Gottschall *et al.* (CBELSA/TAPS Collaboration), Phys. Rev. Lett. **112**, 012003 (2014).

[30] A. Thiel *et al.* (CBELSA/TAPS Collaboration), Phys. Rev. Lett. **109**, 102001 (2012).

[31] O. Bartalini *et al.*, Eur. Phys. J. A **26**, 399 (2005).

[32] http://gwdac.phys.gwu.edu/

[33] C. de Boor, *A Practical Guide to Splines* (Springer-Verlag, Heidelberg, 1978), revised (2001).

[34] I. G. Aznauryan, Phys. Rev. C **67**, 015209 (2003).

[35] B. Pasquini, D. Drechsel, and L. Tiator, Eur. Phys. J. A **27**, 231 (2006).

[36] I. S. Barker, A. Donnachie, and J. K. Storrow, Nucl. Phys. **B 95**, 347 (1975).

[37] R. L. Walker, Phys. Rev. **182**, 1729 (1969).